Energy 72 (2014) 443–458

Contents lists available at ScienceDirect

Energy

journal homepage: www.elsevier.com/locate/energy

Features of a fully renewable US electricity system: Optimized mixes of wind and solar PV and transmission grid extensions

Sarah Becker [a, b, *], Bethany A. Frew [b], Gorm B. Andresen [d, b], Timo Zeyer [c], Stefan Schramm [a], Martin Greiner [d, e], Mark Z. Jacobson [b]

[a] Frankfurt Institute for Advanced Studies, Goethe-Universität, 60438 Frankfurt am Main, Germany
[b] Department of Civil and Environmental Engineering, Stanford University, Stanford, CA, USA
[c] Department of Physics, Aarhus University, 8000 Aarhus C, Denmark
[d] Department of Engineering, Aarhus University, 8200 Aarhus N, Denmark
[e] Department of Mathematics, Aarhus University, 8000 Aarhus C, Denmark

ARTICLE INFO

Article history:
Received 31 January 2014
Received in revised form
15 May 2014
Accepted 17 May 2014
Available online 18 June 2014

Keywords:
Energy system design
Large-scale integration of renewable power generation
Wind power generation
Solar PV power generation
Power transmission

ABSTRACT

A future energy system is likely to rely heavily on wind and solar PV. To quantify general features of such a weather dependent electricity supply in the contiguous US, wind and solar PV generation data are calculated, based on 32 years of weather data with temporal resolution of 1 h and spatial resolution of 40×40 km^2, assuming site-suitability-based and stochastic wind and solar capacity distributions. The regional wind-and-solar mixes matching load and generation closest on seasonal timescales cluster around 80% solar share, owing to the US summer load peak. This mix more than halves long-term storage requirements, compared to wind only. The mixes matching generation and load best on daily timescales lie at about 80% wind share, due to the nightly gap in solar production. Going from solar only to this mix reduces backup energy needs by about 50%. Furthermore, we calculate shifts in FERC (Federal Energy Regulatory Commission)-level LCOE (Levelized Costs Of Electricity) for wind and solar PV due to differing weather conditions. Regional LCOE vary by up to 29%, and LCOE-optimal mixes largely follow resource quality. A transmission network enhancement among FERC regions is constructed to transfer high penetrations of solar and wind across FERC boundaries, employing a novel least-cost optimization.

1. Introduction

CO_2 and air pollution emission reduction goals as well as energy security, price stability, and affordability considerations make renewable electricity generation attractive. A highly renewable electricity supply will be based to a large extent on wind and solar photovoltaic (PV) power, since these two resources are both abundant and either relatively inexpensive or rapidly becoming cost competitive [1]. Such a system demands a fundamentally different design approach: While electricity generation was traditionally constructed to be dispatchable in order to follow the demand, wind and solar PV power output is largely determined by weather conditions that are out of human control. We therefore collectively term them VRES (variable renewable energy sources). Spatial aggregation has a favorable impact on generation characteristics, as was found both for wind and solar PV power in numerous studies [2–9]. Especially for wind, smoothing effects are much more pronounced on large scales, as can be seen from the comparison of the US East coast (about 3000×500 km^2), discussed in Ref. [8], to Denmark (about 200×300 km^2), cf. Ref. [9]. In spite of the leveling effects of aggregation, there is still a considerable mismatch between load and generation left, which is partly due also to load variability.

This paper aims to identify general design features for the US power system with a high share of wind and solar PV. While several studies have demonstrated the feasibility of high penetrations of VRES generators in the regional or nationwide US electric system [11–14], these have only evaluated one individual US region and/or have only considered a small set of hours for their analysis. This paper is based on data for the entire contiguous US of unprecedented temporal length and spatial resolution. Relying on 32 years of weather data with hourly time resolution and a spatial resolution of 40×40 km^2, potential future wind and solar PV generation time

* Corresponding author. Frankfurt Institute for Advanced Studies, Goethe-Universität, 60438 Frankfurt am Main, Germany.
E-mail address: becker@fias.uni-frankfurt.de (S. Becker).

http://dx.doi.org/10.1016/j.energy.2014.05.067
0360-5442/

series are calculated and compared to historical load profiles for the entire contiguous US, divided into the 10 FERC (Federal Energy Regulatory Commission) regions (see Fig. 1).

Similar studies concerning single European countries like Denmark [15] or Ireland [16] comprise the work of the EnergiPLAN group in Denmark. They model renewable energy systems in more detail, but with a smaller weather data basis and without transmission. On the other hand, Refs. [17, 18] investigate a renewable European future with a special focus on transmission grid extensions. Further work has been performed by some of us previously for Europe, [19–23], starting from detailed weather data and deriving general features of the electricity system. An analysis of the Australian power system, focusing attention on economics in a carbon-constrained world, can be found in Refs. [24, 25].

We present two example applications of the obtained generation data: First, it is examined how the mix of wind and solar power can be tuned to reduce the usage of back-up power plants and storage, and second, different transmission grid extensions and their effects are investigated. Both issues are first addressed on a purely technical level, where our only concern is the reduction of back-up or storage energy needed, and then on an economical level, taking costs of wind and solar PV installations and of transmission lines into account. These costs are resolved on a FERC region level to account for spatial differences.

Comparisons between technically optimal systems and cost-optimal developments allow us to judge the effect of costs as well as cost uncertainties on our projections. For the mix between wind and solar PV power, we investigate different relative costs in detail and show their impact on the optimal mix. For transmission, we confine ourselves to two cost scenarios due to computational limitations, and compare them to a heuristic approach used previously.

This paper is organized as follows: Section 2 describes the input weather data set, and how wind and solar generation time series are obtained from it. Section 3 describes the load data as well as the mismatch between VRES generation and load. Sections 4 and 5 present the two applications of the generation and load data set: Calculation of the optimal mix between wind and solar PV with respect to several objectives in Section 4, and an optimal enhancement of the transmission grid for sharing VRES among the FERC regions in Section 5. Section 6 concludes the paper.

2. Weather and generation data

As data basis for the generation time series of wind and solar PV, we use the renewable energy atlas developed in [26]. It is based on weather data from NCEP CFSR for the years 1979-2010 [27], with

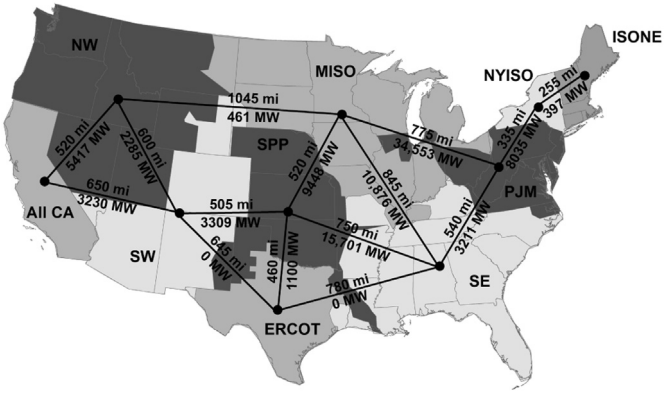

Fig. 1. FERC (Federal Energy Regulatory Commission) regions in the contiguous US. Geographical center points, their distances, and the installed transmission capacity as of 2008 are included. Data as compiled in Ref. [10].

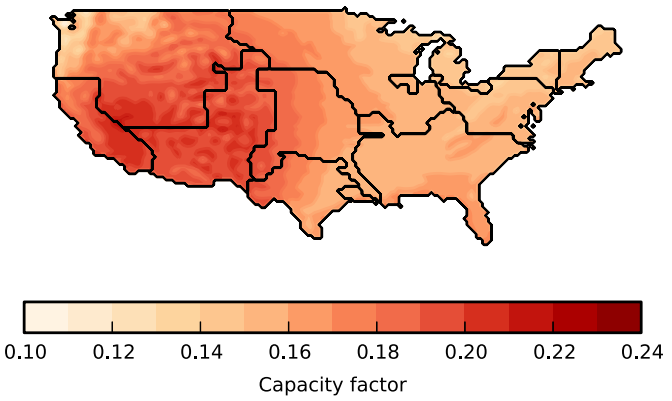

Fig. 2. Solar resource map for the contiguous US as calculated from the renewable energy atlas [26].

hourly time resolution and an area of approximately 40×40 km^2 in each grid cell, covering the contiguous US. The conversion from weather data to potential wind and solar PV generation is done on a grid cell level and then aggregated to FERC region level.

By aggregating time series of wind and solar power, we implicitly assume that the FERC region-internal transmission system is essentially unconstrained. This is reasonable for an electricity system with a high share of VRES, since aggregation of wind and solar power smooths the total output [2–9], and hence there is a strong incentive to remove bottlenecks in the transmission grid. For now, we only assume aggregation on FERC level. The inter-FERC transmission grid will be considered explicitly in Section 5.

2.1. Solar PV power

Solar power production is calculated from weather data as detailed in [26], assuming non-tracking, south-oriented solar panels of the type Scheuten 215 I [28] with a tilt equal to latitude. The corresponding resource map is shown in Fig. 2. It agrees very well with the respective solar PV resource map from the National Renewable Energy Laboratory (NREL) [29].

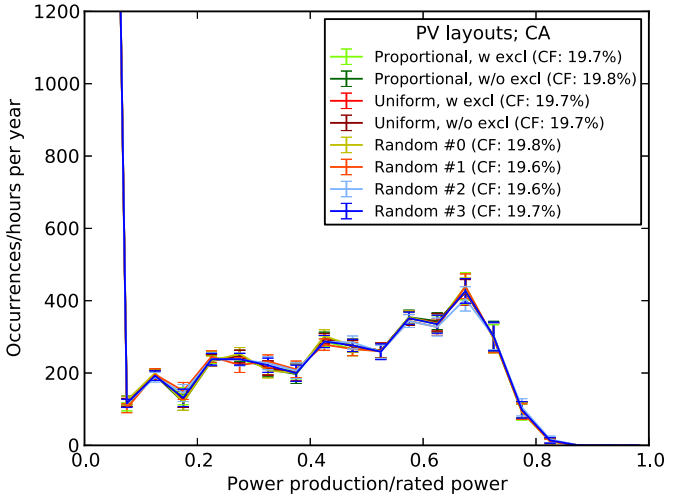

Fig. 3. Solar power output histogram for California, for eight capacity layouts: Proportional to potential generation, not taking any excluded areas into account, proportional to potential generation, taking excluded areas from Refs. [30,31] into account, uniform distribution with and without excluded areas, and four random layouts, in which solar power capacity is distributed randomly to 10% of all grid cells. In the legend, the CF (capacity factor) of the layout that is achieved throughout the years is shown along with the layout name.

The actual production within a FERC region is then determined by applying a capacity layout to the grid cells, i.e. deciding how much capacity is installed in each grid cell and summing up the output from all cells, weighted with this layout. The validation plot Fig. 3 shows the resulting generation time series' production statistics for eight different capacity layouts: Uniform distribution of PV capacity and distribution proportional to the potential solar energy output both with or without exclusion of areas that are declared unsuitable and/or prohibited according to [30, 31], and four layouts in which the PV capacity is assigned randomly to 10% of the grid cells. The night hours amount to a peak a zero production. The plot reveals that the choice of capacity layout does not have a large effect on the (normalized) solar generation time series. The spread in capacity factor is only 0.2% for the example region of California shown in the plot. For FERC regions in which the resource is less homogeneously distributed, such as ERCOT or NW, a slightly larger spread of about 0.5% is observed. To make a realistic guess for the layout, we assume a capacity distribution proportional to the potential of the grid cell under consideration with exclusion of unsuitable areas. The solar capacity layout looks therefore very similar to the solar potential map Fig. 2.

2.2. Wind power

Wind speed interpolation from 10 m wind data to hub height is used:

$$u(H) = u(10\text{ m})\frac{\ln\left(\frac{H}{z_0}\right)}{\ln\left(\frac{10\text{ m}}{z_0}\right)}, \quad (1)$$

where H is the hub height, z_0 is the surface roughness, and u is the wind speed as a function of height. This vertical extrapolation tends to underestimate hub wind speeds slightly, as discussed in [32]. Their research indicates that it would be better to use measurement data from soundings. However, since such data are not available for the entire US, the simple conversion method of Eq. 1 is employed. A hub height of 80 m onshore and 100 m offshore is chosen. To convert the wind speed at hub height to power output, the power curve of the Vestas V90 3 MW turbine is used onshore, and the Vestas V164 7 MW turbine offshore, as provided by the manufacturer [33]. These relatively new and large models were chosen since the main aim of this study is the investigation of a far future, highly renewable energy system. The wind resource map thus obtained is shown in Fig. 4, which aligns reasonably well with the resource maps from NREL [29]. The conversion from wind speed data to wind power generation was modified with the methods of [34, 35] to take effects of orography, surface roughness, and siting into account, see Appendix A for details.

For wind, the sensitivity to siting is substantially higher than for PV, as is observed from the spread in the production distribution for different capacity layouts for wind (Fig. 5), which is large compared to the corresponding Fig. 3. We therefore rely on the wind capacity layouts given by the Eastern and Western wind studies of NREL [30, 31], which include extensive siting analysis. Their layouts do not cover the FERC regions ERCOT and SE very well. For these two regions, we use a randomized layout. The wind power output distribution from eight different candidate layouts for SE is shown in Fig. 5, which compares power output statistics. All of them are randomly generated by distributing a number of capacity units across all available grid cells, proportional to their potential wind power output squared or cubed (cf. the legend of Fig. 5). The higher the exponent on the potential wind output, the more high-yield sites are preferred. The amount of capacity units is a handle on how smooth the layout becomes: The fewer units, the more grained the final layout. It is chosen between 40% and 100% of the number of available grid cells. Grid cells are allowed to hold more than one unit of capacity, so even in a layout using 100% of all grid cells as the number of capacity units, not all grid cells are covered. Since the power output is normalized, only the relative capacity fraction assigned to each grid cell is important. The layout picked for SE and ERCOT in this analysis uses 40% of all grid cells in capacity units, distributed proportional to the cube of potential wind power output. It can be seen in Fig. 6 to match well the distribution of wind sites in the rest of the US.

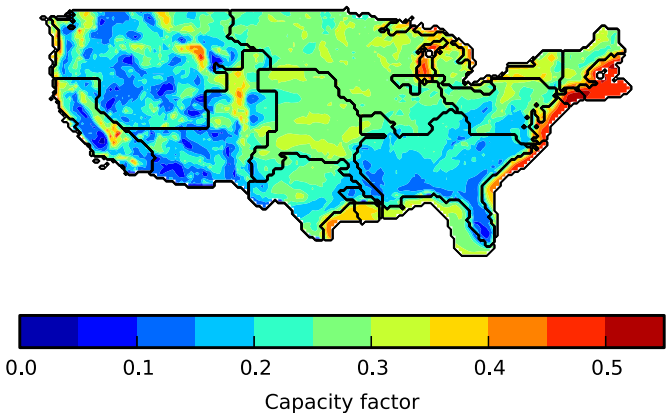

Fig. 4. Wind resource map for the contiguous US as calculated from the renewable energy atlas [26], modified as described in Appendix A to take effects of orography, surface roughness, and siting into account.

The mix between on- and offshore wind is chosen such that the relative capacity between the two is the same as in the NREL wind studies [30, 31], see Table 1 for the values used. Wind installations in the Great Lakes have been treated as offshore, i.e. the offshore 7 MW turbine are assumed to be installed.

3. Load data and mismatch

Actual, historical (2006-2007) load data on the FERC region spatial scale with hourly temporal resolution from the TSOs

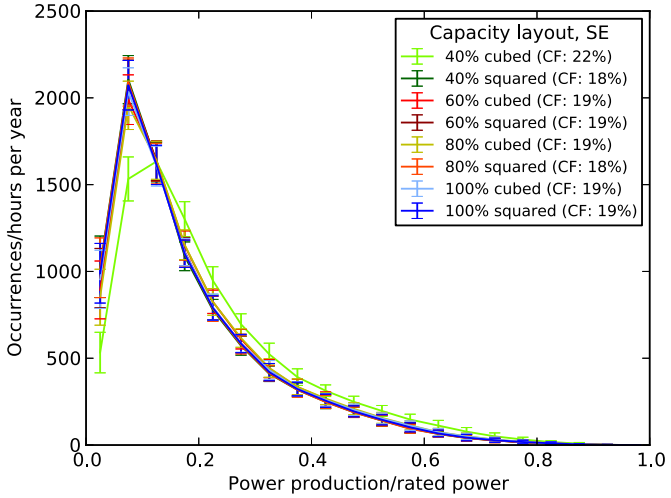

Fig. 5. Wind power output distribution and capacity factors for different capacity layouts for the SE FERC region. The layouts are chosen randomly, with probability of picking a grid cell proportional to its wind potential squared or cubed as stated in the legend, and the total capacity was split into more or fewer units to be randomly distributed (percentage value in the legend), see Section 2.2 for a detailed explanation.

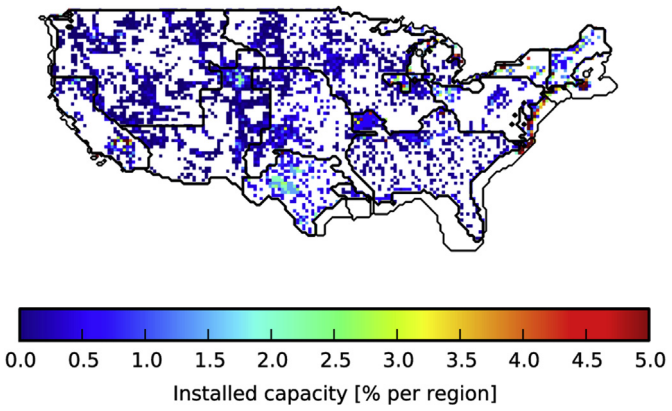

Fig. 6. Wind capacity layout for the contiguous US used in this study. White cells do not contain any capacity. For the colored cells, color encodes the amount of capacity in percent of the installed capacity per FERC region. The 200 m bathymetry line is shown offshore. For most FERC regions, a merger of the wind capacity layouts of Refs. [30,31] is used. For SE and ERCOT, this is not possible due to a very low number of sites in these two FERC regions in both NREL datasets. We therefore use a synthetic random layout in SE and ERCOT, distributing a number of 40% of the number of grid cells in the region of capacity units over all grid cells. The probability of picking a specific cell is chosen proportional to its potential power output cubed, and putting more than one capacity unit into a grid cell was allowed. See Section 2.2 for a detailed explanation. This layout is seen to match the distribution of capacity across the rest of the US well.

(transmission system operators) as compiled in [10] serves as the third ingredient to calculate the hourly mismatch between VRES generation and load on FERC region level:

$$\Delta_n(t) = \gamma_n\left(\alpha_n^{\mathrm{W}} G_n^{\mathrm{W}}(t) + \left(1-\alpha_n^{\mathrm{W}}\right) G_n^{\mathrm{S}}(t)\right)\cdot\langle L_n\rangle - L_n(t) \qquad (2)$$

In this equation, $G_n^{\mathrm{W}}(t)$ and $G_n^{\mathrm{S}}(t)$ are the wind and solar PV generation, respectively, in FERC region n, at time t, normalized to an average of unity. $L_n(t)$ is the load in FERC region n, at time t, in MW, and $\langle L_n\rangle$ is its time average. γ_n is the renewable penetration, i.e. the gross share of VRES. It is used as a scaling factor to model different stages of the VRES deployment. Finally, α_n^{W} is the relative share of wind in VRES.

The load data are extended by repetition to cover the entire timespan of wind and solar data of 32 years. To this end, the load of the SW FERC region was de-trended by removing a net linear growth such that the end of 2007 and the beginning of 2006 fit together. For all other FERC regions, this was not necessary.

4. Optimal mixes

As a first example application of the obtained US wind and solar generation data, we look at three different ways of optimizing the mix between wind and solar PV: minimizing storage energy capacity, minimizing system imbalance energy, and minimizing levelized costs of renewable electricity generation. The mixes are all calculated for a fully renewable scenario, i.e. a VRES gross share of 100%, in a scenario where each FERC region operates independently (that is, no inter-FERC transmission) as well as for full aggregation across the entire US (corresponding to unlimited transmission). First, we minimize storage energy capacity in the case of no other sources of back-up energy. Then, we minimize system imbalance in the case where this imbalance is provided by weather-independent dispatchable generators without storage. Finally, we minimize wind and solar levelized cost of electricity (LCOE), taking the regionally-adjusted costs of wind and solar PV into account, again with dispatchable back-up generation and without storage. Collectively, these three cases give us insight into how the optimal wind and solar mix for a fully renewable US electric system varies for different system criteria, and what benefits are to be gained by adjusting the wind/solar mix.

Table 1
Relative fraction of on- and offshore wind power installations for the layouts used in this study, for each FERC region separately.

Region	Onshore fraction	Offshore fraction
AllCA	98.2%	1.8%
ERCOT	100.0%	0.0%
ISONE	45.8%	54.2%
MISO	97.6%	2.4%
NW	99.9%	0.1%
NYISO	60.8%	39.2%
PJM	42.3%	57.7%
SE	100.0%	0.0%
SPP	100.0%	0.0%
SW	100.0%	0.0%

4.1. Minimizing storage energy capacity

A scenario is considered where each of the FERC regions is isolated from the others and each of them have reached a VRES gross share of 100%, $\gamma_n = 1 \ \forall n$ in Eq. (2). For comparison, the analogous results for an aggregation across the entire US is calculated as well. We look at an electricity system where all the surplus generation (positive mismatch in Eq. (2)) is put into an idealized, 100% efficient storage system and all deficits are covered by re-extracting the stored energy. Since VRES generation equals on average the load and storage losses are neglected, such a system provides enough power at all times.

Our objective is to minimize the storage energy capacity E_n^H. It can be calculated from the storage filling level time series $H_n(t)$ as follows:

$$\begin{aligned} H_n(t) &= H_n(t-1) + \Delta_n(t) \\ E_n^H &= \max_t(H_n(t)) - \min_t(H_n(t)) \end{aligned} \qquad (3)$$

The storage optimal mix for FERC region n is defined to be the α_n^{W} that minimizes this quantity.

The mix minimizing storage energy capacity needs is heavily leaning toward solar PV power, leading to almost exclusive use of solar for the southernmost FERC regions, see Fig. 7a. This is due to the general trend that solar irradiation shows less seasonal variation close to the equator, and is therefore more favorable in terms of storage needs, since these are mainly determined by seasonal timescales, as was observed and analyzed in Ref. [20]. Additionally, the load in most of the US peaks in summer due to air conditioning needs. It is thus correlated with the solar PV power output, further shifting the US storage optimal mix toward solar PV. This mix may change when the seasonal load pattern in the US changes, which may happen, e.g. due to more electrical vehicles being used and needing to be charged throughout the year. In contrast to the US, wind gains a higher share in the European storage optimal mixes, which are on the order of 50–60% wind power [20]. This is due to two effects: The load in Europe peaks in winter due to heating and illumination needs and is thus anti-correlated to solar PV, and because of the higher latitudes, the seasonal variation in solar PV output is more pronounced. The aggregation of the entire contiguous US favors a higher share of wind, as shown in the leftmost bar of Fig. 7a.

From Fig. 7a, it is apparent that the sensitivity of the storage energy capacity to the mix is not very pronounced: A large change in the mix leads to a rather small change in storage energy capacity. The error bars in Fig. 7a indicate mixes that lead to storage energy capacities larger than the optimum by 1% of the load. They spread across 10% to 25% relative share.

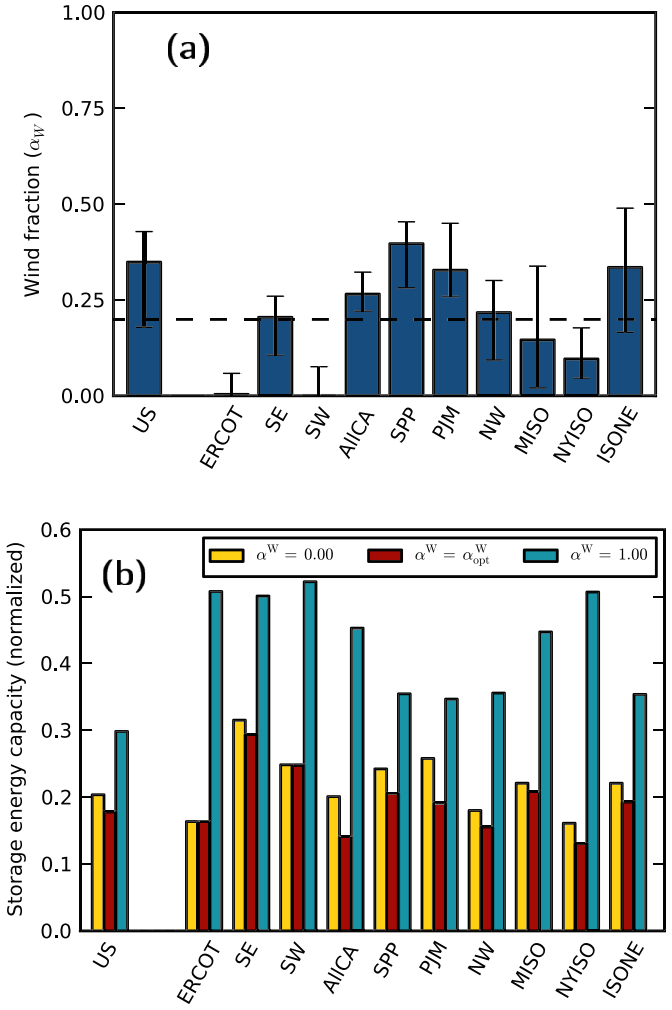

Fig. 7. (a): Storage optimal mix between wind and solar power, given as the percentage of wind power, for the contiguous US FERC regions as well as their aggregation (marked "US"), at 100% renewable penetration. This mix leads to minimal storage energy capacity needs (assuming that all residual loads have to be covered from a stored surplus; no storage losses). The error bars indicate mixes that lead to a storage energy capacity that is larger by 1% of the load than for the storage optimal mix. The dashed line marks the weighted average of the storage optimal mixes across all FERC regions. (b): Storage energy capacity, normalized by the average annual load, for different mixes of wind and solar PV power: Solar PV only, the storage optimal mix, and wind only.

The optimal storage energy capacity shown in Fig. 7b is around two to three months of average load, which is comparable with European values [20]. This figure also shows that a wind-only power system has a highly unfavorable effect on storage capacities needed, roughly tripling the storage needs in extreme cases such as ERCOT and, interestingly, also NYISO, which has very good wind resource quality, cf. Fig. 4.

4.2. Minimizing balancing energy

In this case, no storage is assumed to be in place. Instead, whenever the mismatch (2) is negative, the residual load has to be covered from other, dispatchable power sources. We collectively term these "balancing", B, since they balance the electricity system.

This scenario prompts a different plausible objective to determine the optimal mix α_n^W of wind and solar power: Minimize the total amount of balancing energy $\sum_t B_n(t)$:

$$\sum_t B_n(t) = \sum_t (\Delta_n(t))_- = \sum_t \left[\gamma_n\left(\alpha_n^W G_n^W(t) + \left(1-\alpha_n^W\right)G_n^S(t)\right)\langle L_n\rangle - L_n(t)\right]_- \quad (4)$$

as a function of α_n^W, where $[x]_- = \max\{-x, 0\}$ denotes the negative part of a quantity x.

In Fig. 8a, the balancing optimal mix between wind and solar power is shown for the contiguous US FERC regions. It is seen that the mix minimizing residual load is around 80% wind, almost homogeneously distributed throughout the country. Again, for the aggregated contiguous US, the share of wind is seen to rise, in this case to 90%. This is due to long-range decorrelation effects in the range of 500 km to 1000 km [7, 8]. The total balancing energy necessary is shown in Fig. 8b. Single-region values range from a little less than 25% to about 30% of the annual load. In the case of balancing energy minimization, the solar PV-only mix is found to perform worst, which is due to the need for balancing whenever the sun does not shine, that is, every night. Both the balancing optimal mix and the optimal balancing energies are similar to what

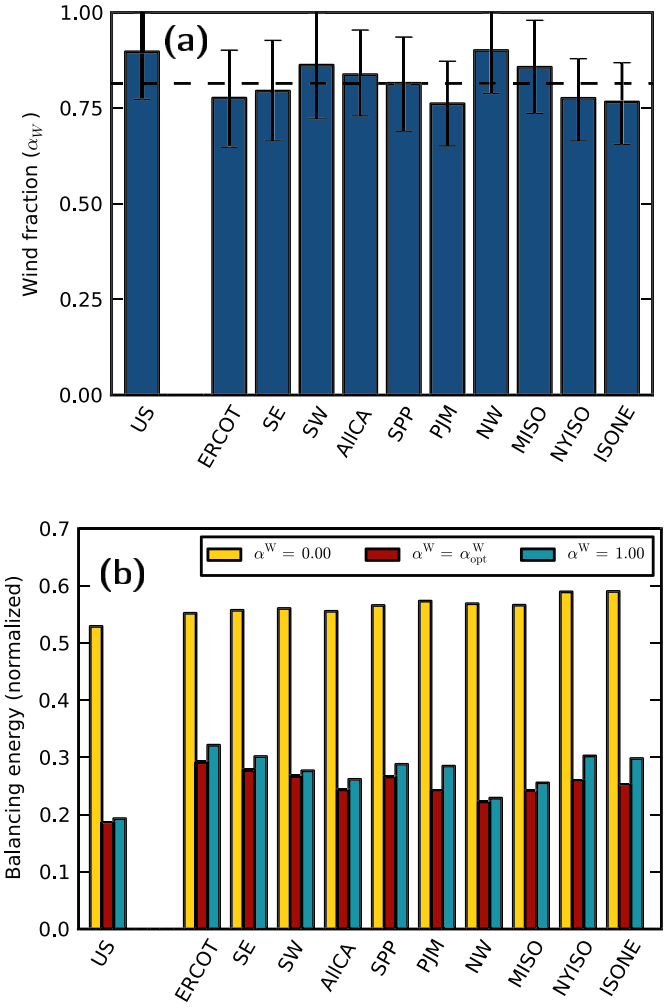

Fig. 8. (a): Balancing optimal mix between wind and solar power, given as the percentage of wind power, for the contiguous US FERC regions, at 100% renewable penetration. This mix minimizes balancing energy or equivalently, residual load. The error bars extend to mixes that would lead to one additional percent of the total load being covered from dispatchable sources. The dashed line indicates the weighted average of the balancing optimal mix across all FERC regions. (b): Balancing energies for different mixes: Solar PV only, the balancing optimal mix, and wind only.

has been calculated earlier with the same method for Europe [22]. The only noticeable deviation occurs in the fully aggregated case, where for Europe optimal balancing energies as low as 15% of the annual load have been found, compared to 18% for the contiguous US, see also Section 5.1.

4.3. Minimizing LCOE from VRES

We now calculate an optimized mix of wind and solar PV power based on their LCOE (levelized costs of electricity). As in Section 4.2, the contiguous US with 100% gross share of VRES are considered ($\gamma_n = 1$). It is assumed that no storage system is in place. Surplus generation (positive $\Delta_n(t)$ in Eq. (2)) is curtailed, while insufficient generation has to be balanced by dispatchable power.

4.3.1. Regional LCOE

The storage and balancing optimal mixes discussed above are based solely on the temporal characteristics of the wind and solar generation. They do not take the capacity factor into account, i.e. the ratio of the average generation of a solar panel or wind turbine under the conditions at a given site to its nameplate capacity. This number, however, determines how large an installation needs to be in order to generate a certain amount of electrical energy, and is consequently a major constituent of the total energy costs. Furthermore, the cost of labor, materials and equipment varies locally across the US, leading to extra regional differences in investment costs. We have developed a model to incorporate these effects. Additionally, it is able to handle different US average wind and solar LCOE.

First, regional LCOE variations due to capacity factor differences are included by using the inverse capacity factors CF_n as weights w_n. The costs of an installation per unit of power are largely independent of the number of units of energy generated. Since the cost is distributed evenly over all units of energy generated, the cost of a single unit is directly anti-proportional to the number of units generated. The weights are normalized to keep the average price at input level.

$$w_n = \frac{\mathrm{CF}_n^{-1}}{\sum_m \mathrm{CF}_m^{-1}/10}$$

Second, different labor, equipment, and materials costs in different FERC regions are taken into account using the method described in [36] with input data from [37]. This yields regional multipliers m_n on the order of one for each of the FERC regions. Put together, this results in a local LCOE of

$$\mathrm{LCOE}_n = m_n w_n \cdot \mathrm{LCOE}_{\mathrm{avg}}, \tag{5}$$

where $\mathrm{LCOE}_{\mathrm{avg}}$ is the average LCOE of the technology under consideration. This cost regionalization is done twice independently, once for wind and once for solar. The cost factors as well as the regional LCOE can be found in Table 2. It is observed that solar installations have lowest costs in the southern and western regions, while they are expensive on the northern East Coast, and vice versa for wind costs.

4.3.2. Calculation of the LCOE-optimal mix

The regional LCOE of wind and solar are then combined and modified to include the effects of curtailment by multiplying them by the ratio of generated to used energy:

$$\mathrm{LCOE}_0\left(\alpha_n^{\mathrm{W}}\right) = \alpha_n^{\mathrm{W}}\mathrm{LCOE}_n^{\mathrm{W}} + \left(1-\alpha_n^{\mathrm{W}}\right)\mathrm{LCOE}_n^{\mathrm{S}} \tag{6}$$

Table 2
Regional LCOE with corresponding regional capacity and weight factors, as well as the deviation from the average LCOE in percent, for wind (top) and solar (bottom). The US average LCOE for both wind and solar PV is assumed to be 0.08 $/kWh. Note that the NW FERC region also comprises Nevada and Utah (cf. Fig. 1), thus explaining the low solar LCOE there.

Region	CF_n	w_n	m_n	Dev. from avg.	$\frac{\mathrm{LCOE}_n}{\$/\mathrm{kWh}}$
AllCA	0.25	1.15	1.04	20%	0.096
ERCOT	0.24	1.24	0.97	20%	0.096
ISONE	0.42	0.70	1.02	−29%	0.057
MISO	0.30	0.97	1.00	−3%	0.077
NW	0.25	1.17	1.00	17%	0.094
NYISO	0.36	0.80	1.04	−16%	0.067
PJM	0.37	0.80	1.01	−19%	0.064
SE	0.23	1.27	0.98	24%	0.099
SPP	0.31	0.93	0.98	−8%	0.073
SW	0.30	0.97	0.99	−4%	0.077
avg.	0.30	1.00	1.00	0%	0.080
Region	CF_n	w_n	m_n	Dev. from avg.	$\frac{\mathrm{LCOE}_n}{\$/\mathrm{kWh}}$
AllCA	0.20	0.87	1.04	−10%	0.072
ERCOT	0.18	0.98	0.97	−5%	0.075
ISONE	0.15	1.12	1.02	14%	0.091
MISO	0.17	1.03	1.01	4%	0.083
NW	0.19	0.91	1.00	−9%	0.072
NYISO	0.15	1.15	1.10	26%	0.100
PJM	0.16	1.10	1.03	14%	0.090
SE	0.16	1.05	0.94	−1%	0.079
SPP	0.18	0.94	0.96	−9%	0.072
SW	0.20	0.84	0.98	−17%	0.066
avg.	0.17	1.00	1.00	0%	0.080

$$\mathrm{LCOE}_{\mathrm{mod}\cdot}\left(\alpha_n^{\mathrm{W}}\right) = \mathrm{LCOE}_0\left(\alpha_n^{\mathrm{W}}\right)\cdot\frac{E_{\mathrm{generated}}\left(\alpha_n^{\mathrm{W}}\right)}{E_{\mathrm{generated}}\left(\alpha_n^{W}\right) - E_{\mathrm{curtailed}}\left(\alpha_n^{\mathrm{W}}\right)} \tag{7}$$

This reflects that the LCOE are incurred for all the energy generated, but only recovered by sales of the non-curtailed part (in an idealized economy where retail prices equal the LCOE). Surplus generation thus becomes undesirable in this formulation, because it leads to an effective rise in LCOE.

4.3.3. LCOE-optimal mix

If the LCOE of wind and solar are equal in a given FERC region, the LCOE optimal mix reduces to the balancing minimization discussed in Section 4.2. In this case, LCOE_0 in Eq. (7) becomes independent of the mix, and since the total generated VRES energy $E_{\mathrm{generated}}$ is constant, the optimum is found when $E_{\mathrm{curtailed}}$ is minimal. Since the average VRES generation equals the average load, the total curtailed energy is equal to the total balancing energy, and therefore minimal curtailment and minimal balancing are equivalent here.

We first investigate a case where wind and solar power have the same average LCOE of 0.08 $/kWh (before taking the regionalization from Eq. (5) or the curtailment corrections from Eq. (7) into account). Due to the regionalization of LCOE, this translates into different LCOE in the different FERC regions, and thus we do not simply reproduce the results of Section 4.2. Comparing the regional LCOE optimal mixes shown in Fig. 9a to the balancing optimal mixes in Fig. 8a, we see a shift of the mix toward wind in the North East (particularly in ISONE and NYISO), where wind resources are very good and local wind LCOE are thus low, while it is shifted toward solar in the South (particularly in ERCOT, SE and AllCA) because of the good solar resources there.

The LCOE of different mixes (LCOE-optimal, solar only and wind only) is shown in Fig. 9b. It is apparent that picking the LCOE-optimal mix is able to reduce average LCOE significantly,

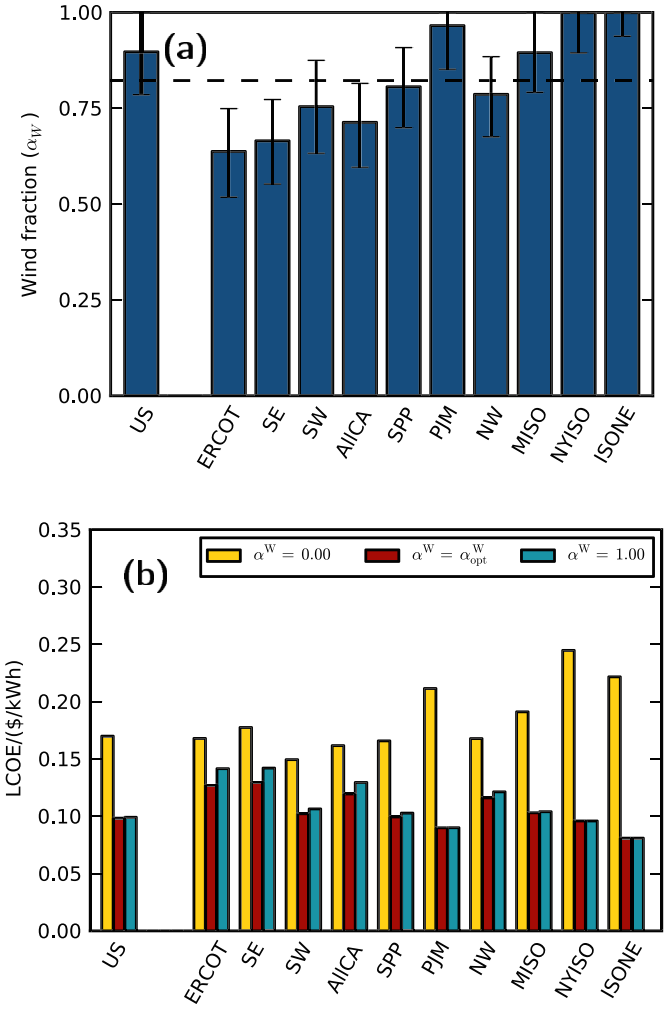

Fig. 9. (a) LCOE-optimal mixes for the case of equal average wind and solar LCOE of 0.08 $/kWh, calculated as described in Sections 4.3.1 and 4.3.2. Note that (a) does not reproduce Fig. 8, because although the mean LCOE for wind and solar are the same here, they are not the same for all FERC regions. (b) Corresponding LCOE in the FERC regions as well as on an aggregated level (denoted "US"), of different wind and solar mixes: Solar PV only, LCOE optimal mix, and wind only.

especially compared to solar-only scenarios. For example, for the entire US, solar only is 70% more expensive than the optimal mix, and for the North East, it is more than twice as expensive. The LCOE for the aggregated US are about $0.10, as could have been directly predicted from Eq. (7): Since wind and solar LCOE are equal in this case, the LCOE optimal mix equals the balancing optimal mix. As calculated in Section 4.2, the optimal balancing energy, which equals the curtailed energy, is 18% of the load. Eq. (7) thus yields

$$\mathrm{LCOE}_{\mathrm{mod.}} = \mathrm{LCOE}_0 \cdot \frac{1}{1-0.18} = \frac{\$0.08}{0.82} \approx \$0.10.$$

4.3.4. Sensitivity to different average LCOE ratios

Today, wind and solar PV differ significantly in their installation price, and they may continue to do so in the future. Various projections of average LCOE for wind and solar PV power across the US have been compiled by Open Energy Information (OpenEI) [38]. We use the price projections for 2020 from the most recent available reports (from 2012) to illustrate the large LCOE ranges, see Table 3.

The impact of different wind and solar price ratios is depicted in Fig. 10, which shows the regional LCOE-optimal mix as a function of

Table 3
Levelized cost of electricity (LCOE) from various reports, as compiled by Open Energy Information (OpenEI [38]). For wind, only two reports were available, so the average is used instead of the median, and quartiles are not meaningful and therefore omitted. In order to calculate a mean price for wind (on- and offshore), a mix of 25% offshore and 75% onshore installations is assumed.

Technology	LCOE in $/kWh					# of Reports
	Minimum	1st Quartile	Median	3rd Quartile	Maximum	
Wind (onshore)	0.060	–	0.065	–	0.070	2
Wind (offshore)	0.100	–	0.105	–	0.110	2
Wind (75/25 mix)	0.070	–	0.075	–	0.080	2
Solar PV	0.040	0.080	0.120	0.190	0.240	12

the ratio of average LCOE, for the representative FERC regions of AllCA, ISONE, MISO, NW, and SE, as well as for the aggregated US. We see that if wind LCOE are half of the solar LCOE on average, then 100% wind will be the optimal mix for all FERC regions. Conversely, if average solar LCOE are half of the wind LCOE, this does *not* lead to a 100% solar cost optimal mix in all FERC regions, cf. Fig. 10. This is due to the large curtailment and balancing such a mix entails. As seen in Section 4.2, the mix minimizing balancing energy lies around 80% wind. Solar only is very unfavorable because it would lead to large balancing and curtailment needs, even if solar LCOE were much lower than wind LCOE.

Looking at different LCOE combinations, we observe that the results in Fig. 9a (i.e. when solar and wind have the same cost) most closely match those from the NREL Renewable Electricity Futures study [14], which uses a cost-based optimization tool to determine the least-cost portfolio of generators, storage, and transmission for various scenarios of an 80% renewable US electric system. In the NREL study, for the 2050 LCOE values for comparable installed capacity values, wind is more heavily installed in the Great Plains, Great Lakes, Central, Northwest, and Mid-Atlantic areas (roughly corresponding to the MISO, SPP, NW and PJM FERC regions) and solar is more heavily installed in CA, the Southwest, Texas, and the South (roughly corresponding to AllCA, SW, ERCOT, and SE FERC regions).

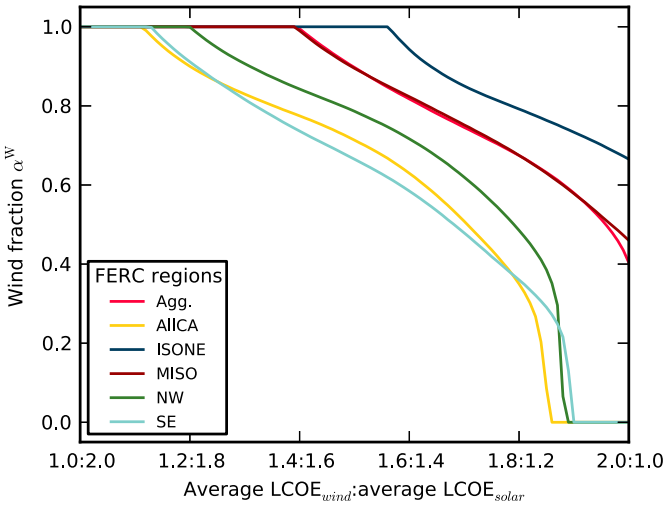

Fig. 10. Cost-optimal wind/solar mixes for five geographically representative FERC regions, for different ratios of the LCOE of wind and solar power. The regional differences in mix due to the climate differences are clearly visible: Southern FERC regions such as AllCA and SE switch to 100% solar if this is much cheaper than wind, while other FERC regions never do. Conversely, if wind is much cheaper, all FERC regions switch to 100% wind power, starting from the northeastern regions, here represented by ISONE.

The high sensitivity of solar PV to prices, relative to that of wind, is corroborated by the significant price impact on solar PV build-out observed in [13]. The NREL Renewable Electricity Futures Study also recognized a high sensitivity of the solar energy (PV and CSP) build-out to varying cost estimates [14]. Furthermore, they found that the relative contributions of wind and solar generation were on average 75% wind to 25% solar across the contiguous US in their optimized scenario. This agrees well with the cost-optimal α^{W} value for equal wind and solar LCOE found here of slightly less than 80%.

5. Optimal transmission grid extensions

After studying different mixes of wind and solar PV power by optimizing various objectives, we now set out to investigate a further component of the electricity system: The role of transmission. In this section, we use the same setting as presented in Section 4.2, that is, the mix between wind and solar PV power is kept at the single node balancing optimal mix, gross VRES share is again 100%, and no storage system is included, such that all deficits have to be covered by balancing.

We first make some general observations and introduce the generalized DC power flow to be used, which is an approximation to the full AC power flow. We then examine three different transmission layouts. Their size is chosen such that they can all be built for a capital investment twice as large as the cost of existing installations. The goal set for transmission grid extensions is that they should reduce balancing energy usage as much as possible. It is not a priori clear how the given investment should be distributed to reinforce single lines in order to achieve this, so we develop different methods of assigning capacity to single links. The first layout is done based on quantiles of the distribution of unconstrained flows analogous to the studies in Refs. [22, 23] for Europe ("Quantile layout"). The second is done by cost optimization for the hypothetical case where all lines have the same costs ("Even layout"). The last one uses cost optimization adopting realistic line cost estimates from Refs. [10, 39] ("Real layout"). The latter two layouts are obtained by the optimization technique of simulated annealing. Our implementation of the algorithm is introduced before the optimized layouts are discussed.

5.1. Maximal balancing energy reduction

The first thing to observe is that the maximal possible balancing energy reduction from transmission can be calculated ad hoc, just by comparing the isolated balancing needs,

$$B_{\mathrm{tot}}^{\mathrm{isolated}} = \sum_t \sum_n [\Delta_n(t)]_-, \tag{8}$$

with the aggregated ones,

$$B_{\mathrm{tot}}^{\mathrm{aggregated}} = \sum_t \left[\sum_n \Delta_n(t) \right]_- . \tag{9}$$

In Eq. (8), all negative mismatches for the different nodes are summed up, yielding the total balancing energy in the case of isolated nodes. Meanwhile, in Eq. (9) the mismatches are first added, thus allowing a negative mismatch at one node to be canceled by a positive one at another. The negative part of this aggregated mismatch, summed over all time steps, gives the minimal possible amount of balancing energy. For the contiguous US, these two numbers are $B_{\mathrm{tot}}^{\mathrm{isolated}} = 25.7\%$ of the total load covered from balancing energy for the isolated case, compared to $B_{\mathrm{tot}}^{\mathrm{aggregated}} = 19.0\%$ in the aggregated case when keeping the wind/solar mixes fixed (no optimization of the mix for the aggregated US as in Section 4.2). Transmission can thus effect a balancing energy reduction by roughly a quarter. Compared to the corresponding scenario for Europe, the isolated nodes (countries in the European case) have to balance around 24% of the total load, which drops to around 15% in the aggregated case, thus a reduction by about two fifths [22]. This indicates that although Europe covers a smaller area, low production phases of wind and solar PV are less correlated there, and hence the aggregated output is smoother than for the US.

5.2. Generalized DC power flow

The flow paradigm introduced and described in Refs. [22, 23] is used to calculate the distribution of balancing as well as the flows on the single links. In this formulation, the standard DC power flow[1], which is a valid approximation for the full AC flow under stable grid conditions, is generalized to cope with flow capacity constraints and global mismatches.

The directed flow along link l is denoted F_l. It is constrained by (possibly direction dependent) power flow capacities $h_{\pm l}$ of the link l,

$$h_{-l} \le F_l \le h_l.$$

Furthermore, we make use of the incidence matrix K which encodes the network topology:

$$K_{\mathrm{nl}} = \begin{cases} 1 & \text{if link } l \text{ starts at node } n \\ -1 & \text{if link } l \text{ ends at node } n \\ 0 & \text{else} \end{cases}$$

Start and end point of each link can be chosen arbitrarily, they only have to be used consistently throughout the calculations. With the help of the flow vector and the incidence matrix, the net outflow from node n can be expressed as

$$\sum_l K_{\mathrm{nl}} F_l.$$

If this quantity is negative, the node experiences a net inflow. The goal is now to find a flow vector $(F_l)_{l=1\ldots L}$ that leads to imports and exports at the single nodes such that deficits and excesses are canceled out at all the nodes, while observing the flow constraints. Since there is in general either a global excess or a global deficit in the grid and the total energy is conserved, it is not possible to reduce all deficits and excesses to zero. Instead, use the following procedure:

$$\min_{h_{-l} \le F_l \le h_l} B_{\mathrm{tot}} = \min_{h_{-l} \le F_l \le h_l} \sum_n \left[\Delta_n - (KF)_n \right]_- = B_{\min} \tag{10}$$

$$\min_{\substack{h_{-l} \le F_l \le h_l \\ \sum_{i=1}^{N} (\Delta_n - (K \cdot F)_n)_- = B_{\min}}} \sum_l F_l^2 \tag{11}$$

In the first step, Eq. (10), the sum of all deficits after imports and exports is minimized. This corresponds to using as little balancing energy or equivalently as much VRE as possible. In the second step, Eq. (11), flow dissipation is minimized, which is proportional to the sum of all the flows squared, while keeping the total deficit at its minimal value found in the first step. This algorithm entails that excesses and deficits at the nodes are matched as locally as possible. For example, if there is a deficit at node A, it is preferred to import to A from nodes in A's neighborhood instead of farther away nodes.

[1] It is termed "DC power flow" in the engineering literature solely due to its formal mathematical analogy with DC flow. We consider AC power flow.

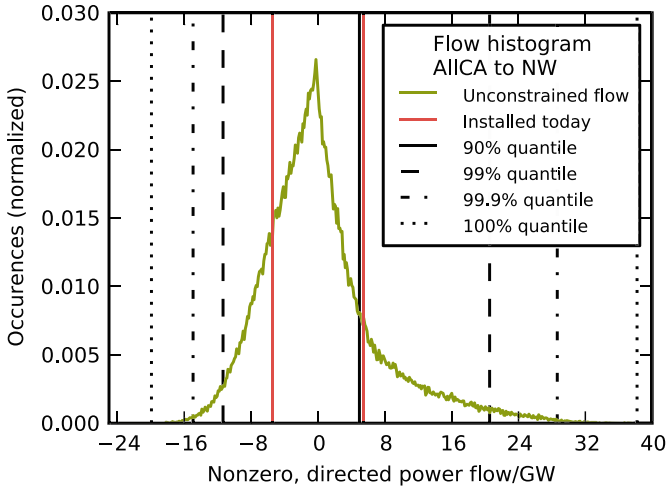

Fig. 11. Unconstrained, directed flow distribution on the example link between AllCA and NW. Vertical lines indicate today's installation (red line), 90% (solid line), 99% (dashed line), 99.9% (dashed–dotted line), and 100% (dotted line) quantiles. Note that in the negative direction (from NW to AllCA), the solid black 90% quantile line is almost covered by today's installation (red vertical line). [For interpretation of color referred in this figure legend, the reader is referred to web version of the article.]

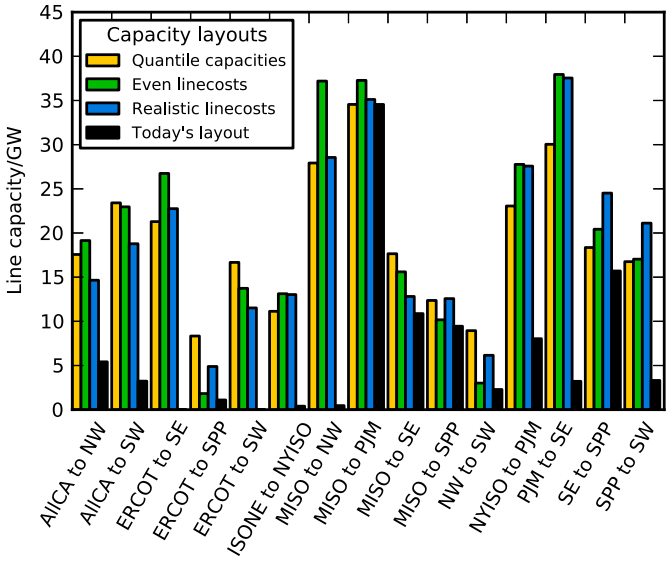

Fig. 13. Quantile line capacity layout and two optimized transmission capacity layouts: if all line costs are assumed equal (Even line costs) and if line cost estimates as given in Table 4 are assumed (Real line costs). In all the layouts, the total investment is set to twice of what is present today, and the total additional line capacity is chosen accordingly. For comparison, today's line capacity layout is shown as well. It serves as a lower bound to the grid extensions.

5.3. Quantile capacity layouts

Neglecting different costs for different lines, the best grid build-up found so far (to our knowledge) is what we term "Quantile line capacities" [22]. These are calculated by first solving the power flow, Eqs. (10) and (11), without the constraint $h_{-l} \leq F_l \leq h_l$, for all hours in the time series. This yields time series for the unconstrained flows on each link, which are binned in a histogram, see Fig. 11 for an example. It has been observed that these unconstrained distributions generally peak around zero and have convex tails, such that a fraction of the line capacity that would be necessary to enable the maximal unconstrained flow is sufficient to let the flow pass through unimpededly most of the time. The Quantile capacities are obtained by taking a certain quantile of the unconstrained flow in each direction and setting the larger of the two as line capacity, for each of the links. In terms of balancing energy reduction, these have been shown to perform much better than, for instance, global scaling of current line capacities [22]. The resulting capacity layout is shown in Fig. 13. The costs of this layout are calculated by taking the realistic cost estimates from Refs. [10,39] (see Table 4) and applying them to the capacity that needs to be added on top of what is installed today to reach the Quantile layout. The quantile for all links is chosen to be 98.36%,

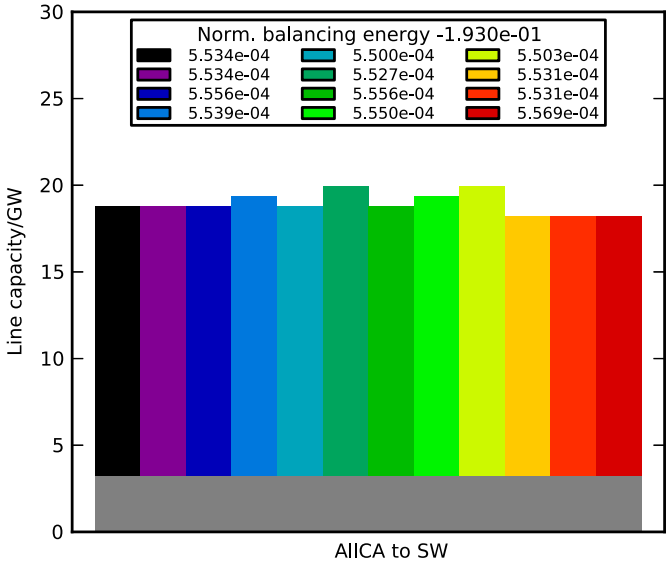

Fig. 12. Optimized link capacities for the representative link between AllCA and SW, for 12 annealing runs from different start points. For the other links, line capacities are similarly close to each other. This plot shows the situation for the realistic line costs, see Section 5.5 for details on the costs. For the even line cost case, the corresponding results resemble this plot. In gray, today's line capacity is overlayed, which serves as a lower bound. The legend shows the resulting balancing energy (minus a constant offset to compare the very similar numbers) as a fraction of the total load, which the different line capacity layouts produce during the 32 years of data.

Table 4
Table of the costs incurred for electricity lines. a_l is the line length in miles, calculated as described in Ref. [10] as the distance between midpoints of the connected FERC regions (see also Fig. 1), b_l is a region-specific, dimensionless line cost multiplier, C_l^{line} is the line cost in $\$_{2006}$ per MW-mi, and $C_l^{\text{async.}}$ is the cost of building AC-DC-AC interties when linking asynchronous regions, in $\$_{2006}$ per kW. Not shown is the constant substation cost of $C_l^{\text{substation}} = 16.3\ \$_{2006}$ per kW. From this input, the total costs in $\$_{2006}$ per MW shown in the last column were calculated. Data are taken from Ref. [39], adjusted to refer to lines (instead of regions) and annualized as described in Ref. [10], assuming an interest rate of 7% and a lifetime of 60 years.

Link	a_l	b_l	C_l^{line}	$C_l^{\text{async.}}$	Total
AllCA-NW	520	2.28	1411	0.0	1.20×10^5
AllCA-SW	650	2.28	1411	0.0	1.50×10^5
ERCOT-SE	780	1.00	1411	216.4	9.50×10^4
ERCOT-SPP	460	1.00	1411	216.4	6.28×10^4
ERCOT-SW	645	1.00	1411	216.4	8.14×10^4
ISONE-NYISO	255	3.56	1129	0.0	7.42×10^4
MISO-NW	1045	1.00	1270	216.4	1.11×10^5
MISO-PJM	775	1.78	1129	0.0	1.12×10^5
MISO-SE	845	1.00	1270	0.0	7.76×10^4
MISO-SPP	520	1.00	1270	0.0	4.82×10^4
NW-SW	600	1.00	1411	0.0	6.15×10^4
NYISO-PJM	335	3.06	1129	0.0	8.37×10^4
PJM-SE	540	1.78	1270	0.0	8.84×10^4
SE-SPP	750	1.00	1411	0.0	7.66×10^4
SPP-SW	505	1.00	1411	216.4	6.73×10^4

Table 5
Percentage of total electricity consumption covered by balancing energy, for the three different line capacity layouts: Quantile capacities, cost optimal line capacities if all lines cost the same (even layout), and for line cost estimates as given in Table 4 (Real layout). For the latter two layouts, the maximal and minimal values across the 12 candidate layouts from the different annealing runs is also shown.

Timespan		32 years	2 years
Layout			
Quantile		19.428%	19.117%
Even	Opt.	19.294%	18.983%
	Min.	19.294%	18.983%
	Max.	19.296%	18.983%
Real	Opt.	19.355%	19.032%
	Min.	19.355%	19.032%
	Max.	19.356%	19.032%

such that in total, the additional investment is twice the cost of today's layout.

5.4. Simulated annealing

While the quantile line capacities lead to layouts that perform well in terms of balancing reduction, they are not optimized. The problem of optimal line capacity distribution does not take the simple form of a convex optimization. Instead, the balancing energy as a function of line capacities appears to be rather complicated in numerical tests, especially when the constraint of a fixed total investment in new lines is taken into account. Simulated annealing is a technique well suited and widely used in physics and related fields for finding minima of such a function [40, 41]. It mimics a physical system settling into its ground state under cooling, where it assumes a (possibly only locally) minimal energy value. In our application, the state of the system corresponds to a given distribution of new line capacity, a line capacity layout or layout, for short. The energy function to be minimized is the total balancing energy B.

The system is started in a random layout. A candidate neighbor layout is chosen by tentatively shifting approximately 100 MW of line capacity from one random link to another. Then, the balancing energy of the neighboring layout is calculated, and a random decision whether to move to the candidate layout is taken. The probability P of switching from the old to the new layout is chosen classically as:

$$P(B_{\text{old}}, B_{\text{new}}, T) = \begin{cases} 1 & \text{if} \quad B_{\text{old}} > B_{\text{new}} \\ e^{-(B_{\text{new}} - B_{\text{old}})/T} & \text{otherwise} \end{cases}, \qquad (12)$$

where B_{old} and B_{new} are the balancing energy of the current and candidate layout, respectively, and T is the temperature parameter, controlling how the space of potential layouts is scanned. If T is large, the transition probability is close to one for any candidate layout, even if B_{new} is much larger than B_{old}, and the system moves like a random walk from layout to layout. For low temperatures, the acceptance probability for shifts to layouts of higher energy goes to zero, and the system performs an almost monotonous descend toward lower balancing energy layouts.

In the runs presented here, T is first kept at a high value to explore the state space. From this first round, twelve start layouts per run are chosen that lead to low balancing energies and lie sufficiently far apart. Next, annealing is performed from these start points, linearly decreasing the temperature to zero. To achieve better results, the best layouts from these runs are reheated to a medium temperature and then recooled. In this way, twelve layouts with very low balancing energy are found. Line capacities for the example link between AllCA and SW are shown in Fig. 12. It is visible that the capacities almost coincide. The same holds true for the other links. Thus it appears that there is one unique line capacity layout minimizing balancing energy. This finding is further corroborated by looking at the spread in balancing energy among the twelve resulting layouts, shown in Table 5. Minima and maxima of balancing energy almost coincide, indicating that there is a single optimal value.

The line capacities present today were enforced as lower bounds. The high temperature was chosen such that typical transition probabilities to a higher balancing energy layout were about 90%, while they reached about 50% at reheating temperatures. The total investment was kept constant by shifting not a fixed amount of line capacity, but line capacity of a fixed cost from one link to the other. Due to computational limitations, the optimization was constrained to the first two years of data.

5.5. Line cost estimates

The realistic line costs estimates are composed of different contributions:

$$C_l = a_l \cdot b_l \cdot C_l^{\text{line}} + C_l^{\text{substation}} + C_l^{\text{async.}}, \qquad (13)$$

where C_l^{line} are the costs of building just the line in $\$_{2006}$/(MW mi), a_l is the line length, b_l a region-specific cost multiplier comprising differences in overall building costs, $C_l^{\text{substation}}$ is the cost of substations per MW, and $C_l^{\text{async.}}$ is the cost of building interties when linking asynchronous regions (the Eastern FERC regions, Western FERC regions, and ERCOT are not synchronized with each other). Cost data come from [39], and are converted to single lines, adjusted to 2006 values and annualized as in [10], assuming a yearly interest rate of $i = 7\%$ and a lifetime of $A = 60$ yrs:

$$C_l^{\text{annualized}} = C_l \cdot \frac{i(1+i)^A}{(1+i)^A - 1}$$

Costs are given in Table 4. Line lengths are approximated by the distances between the geographical center points of the FERC regions they connect. They are shown, together with current transmission capacities, in Fig. 1.

The transmission costs used here are higher than those from Ref. [42] by an average factor of more than five. This is mainly due to the fact that this model assumes links between different FERC regions to be spread out over several lines, which are based on the prevalence of HVAC lines (see Ref. [39] for details), whereas the authors of Ref. [42] assume the entire transmission capacity to be aggregated in a few HVDC lines, which are much less expensive for long-distance lines. For a fair comparison, it has to be noted that the usage of a few HVDC lines for long distance transmission entails more distribution lines from the end-points of these HVDC lines which are not included in long-range transmission in

Table 6
Cost of different line capacity layouts when they are scaled such that they yield the same balancing energy reduction as the quantile capacity layout. Cost calculations have all been done based on the line cost estimates from Table 4. The first row shows the total annual cost. The second row contains the total annual cost normalized by the yearly balancing energy reduction that is achieved (compared to today's layout) by the new line investment. The last row shows the percentage difference in costs with respect to the Quantile layout.

Layout	Quantile	Even	Real
Cost in 10^9 \$/yr	17.99	16.25	16.10
Cost in $\frac{\$/\text{yr}}{\text{MWh/yr}}$	141.02	127.38	126.22
Δ Cost	0.0%	−9.7%	−10.5%

Ref. [42], but which are partly incorporated in our approach since the lines we are considering are distributed. Whether one or the other idea is realized depends on how well the line build-up is coordinated and how concentrated load centers are within the FERC regions linked.

5.6. Optimized line capacity layouts

Cost-optimal line capacity layouts are calculated with simulated annealing for two sets of prices: First, all lines are assigned the same price (an average of the actual cost estimates from Table 4) to obtain the Even layout. It serves as a test of the Quantile line capacities, which should produce very similar results if performing well, as well as a sensitivity check for the second calculation, in which we insert the line cost estimates from Table 4 to produce the Real layout.

The Even and Real line capacity layouts resulting from simulated annealing, as well as the Quantile line capacity layout, are shown in Fig. 13. Quantile line capacities and Even line capacities are generally similar, but differ visibly (compare the yellow and the green bars in Fig. 13). Although they generally are within 2–5 GW of each other, deviations up to 10 GW occur. The performance of the different layouts in terms of balancing energy reduction is shown in Table 5. It is seen that the balancing energy minimization with Even line costs yields lower balancing energies than the Quantile line capacities by more than 0.1% of the total yearly load, or roughly 170 TWh (using 2007 load values). This means that simulated annealing outperforms the Quantile method at the task of optimally distributing a certain amount of additional MW in transmission capacity while neglecting regional differences.

When different line costs enter the game, the line capacity is redistributed to the cheaper links, and thus balancing energy drops not as low as for the Even cost line capacities. It should be noted, however, that the annealing method still reduces balancing energy usage further than the Quantile capacities.

To make a cost comparison between the different capacity layouts without using balancing energy costs which are highly complex and diverse, we scale the Real as well as the Even layout down linearly until they lead to the same amount of total balancing energy as the Quantile layout. The costs of the resulting layouts are then all calculated using the line cost estimates from Table 4, and compared in Table 6. They are reduced by about 10% in both of the optimized layouts, as compared to the Quantile capacity guess.

The additional transmission line capacity for the three cases considered here (Quantile, Even, and Real layout) show large additions along the East Coast (ISONE, NYISO, PJM, and SE FERC regions), West Coast (CA, NW, and SW), and across the boundaries of the three interconnects (ERCOT to adjacent FERC regions; MISO-NW; and SW-SPP), cf. Fig. 14. The grid enhancement in the NREL Futures study (for 2050), Ref. [14], by contrast, is mainly east-west oriented and concentrated in the middle and southwestern areas of the US, with key additions to/from ERCOT, SE, SW, SPP, and MISO FERC regions. These results reflect their greater emphasis on transmitting wind and solar energy from the middle and southwestern areas of the US to large-load, adjacent regions, while in our simulation all FERC regions are assumed to be on average self-supplying, thus reducing the need for transmission.

Table 5 also shows the effect of calculating balancing energy during all available years vs only relying on the first two years. While the shift this introduces is larger than the spread between

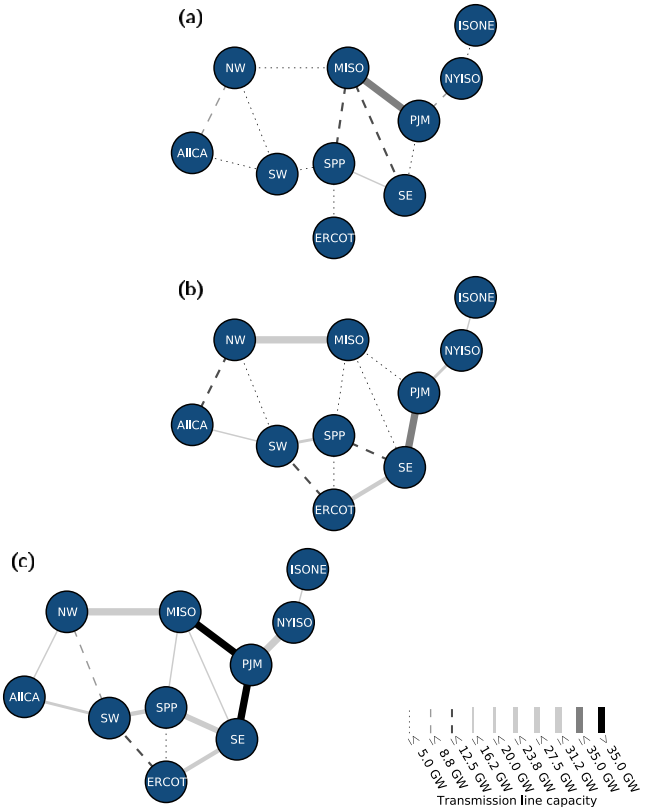

Fig. 14. Today's layout (a) plus additional capacity to realize the Real cost capacity layout (b) gives the Real layout (c). Line thickness and style indicate transmission capacity as described in the legend. Node sizes and positions are not to scale.

the layouts for either 2 or 32 years, it does not affect their relative distances in balancing energy much, and in particular has no impact on their ranking.

6. Conclusions

We introduced a novel, high resolution, long-term dataset for wind and solar PV production in the contiguous US. Possible applications have been demonstrated by calculating the optimal mix of wind and solar PV power with respect to minimizing storage, minimizing balancing energy, and minimizing LCOE. We showed that by picking the right mix, the needs for storage sizes or backup energy can be significantly reduced. Storage energy capacities could be reduced from 30% to 50% of the yearly load for a wind-only mix down to 15% to 20% in a hypothetical storage-only scenario. Balancing energy could be brought down from more than 50% of the yearly load with solar PV only to 20% to 25%, depending on the transmission grid. Furthermore, we investigated the influence of installation and operation costs on the optimal wind-solar mix and showed how sensitive this mix is to relative prices, highlighting the need for reliable price predictions. Again, picking the optimal mix reduced expenses (here LCOE), by a factor of almost two. Interestingly, when taking effects of surplus production that is lost to the system into account, LCOE differences between wind and solar are seen to play an increasingly minor role with rising renewable penetration. The LCOE-optimized mix is instead driven by the avoidance of losses from surplus production, which becomes more important than the installation costs. This can be read as an indication that it pays in the long term to maintain a varied technology mix in spite of different installation costs.

As a second application, we calculated optimized transmission grid extensions, showing the importance of a careful numerical optimization of the grid's capacity layout. Introducing transmission line costs helped to integrate regional differences such as different labor and equipment costs and different line lengths. We showed, however, that the improvement over an ad-hoc assumption of uniform line costs per MW was not very significant, resulting in 0.8% higher costs for the same reduction in balancing energy. This also highlights that our analysis is relatively insensitive to transmission line costs. The main improvement of the study was introducing simulated annealing techniques in optimizing the transmission line capacities, which led to a cost reduction by more than 10% compared to simpler approaches.

Acknowledgments

SB gratefully acknowledges financial support from O. and H. Stöcker as well as M. and H. Puschmann, BAF from a National Defense Science and Engineering Graduate (NDSEG) fellowship, a National Science Foundation (NSF) graduate fellowship, and a Stanford University Charles H. Leavell Graduate Student Fellowship, and GBA from DONG Energy and the Danish Advanced Technology Foundation. Furthermore, we thank Anders A. Søndergaard for helpful and constructive discussions.

Appendix A. Wind conversion

Appendix A.1. Original approach

In a first attempt, the wind conversion was done with the Aarhus RE atlas as described in Ref. [26]. Summarized briefly, the wind speed at hub height was extrapolated from measurements of wind speeds at 10 m height $u(10\,\mathrm{m})$ via

$$u(H) = u(10\,\mathrm{m}) \cdot \frac{\ln(H/z_0)}{\ln(10\,\mathrm{m}/z_0)}, \tag{A.1}$$

where u is the wind speed as a function of height, H is the hub height, and z_0 is the surface roughness. The wind speed was in turn converted into turbine power output with the help of power curves as can be found in data sheets for wind turbines. Specifically, we used data for the model Vestas V90 3 MW with 80 m hub height onshore and for Vestas V164 7 MW with 100 m hub height offshore.

When evaluating the data, it became apparent that this approach significantly underestimates the wind power potential, see Fig. A.17a and c.

Appendix A.2. Modified approach

In order to fix this issue, the methods described in Refs. [34,35] were applied. The main reason that wind power potential is underestimated onshore is that the spatial fluctuations in wind speed due to surface roughness and orography (hills and valleys) is neglected when working with spatially averaged wind speeds. However, these fluctuations contribute to the mean wind energy density, as the following calculation shows:

$$\frac{2\langle e\rangle}{\rho} = \langle u^3\rangle = \langle(\overline{u}+u')^3\rangle \approx \overline{u}^3 + 3\overline{u}\langle u'^2\rangle = \overline{u}^3 + 3\overline{u}\sigma^2 \tag{A.2}$$

where e is the wind energy density, ρ is the mass per volume air density (assumed constant), $\overline{u}$ is the mean wind speed, u' are the spatial fluctuations around $\overline{u}$ such that $u = \overline{u} + u'$, and σ is the standard deviation of u'.

Interestingly, the wind speed fluctuations due to inhomogeneous terrain can be characterized in terms of its surface roughness and orography, yielding

$$\sigma = \sqrt{\sigma_{\mathrm{oro}}^2 + \sigma_{\mathrm{rough}}^2}. \tag{A.3}$$

The details of this connection are given below. The resulting σ is then converted to an effective increase in wind speed, which leads to an increased power output.

With the additional assumption that the distribution of u' is Gaussian, even the effect of siting can be modeled in a simplified way: Wind turbines would primarily be placed in good spots, that is, where u' is larger than some threshold value p. This leads to mean energy densities of

$$\frac{2\langle e\rangle}{\rho} = \langle u^3\rangle = \langle(\overline{u} + u'\cdot\theta(u'>p))^3\rangle, \tag{A.4}$$

where θ is a cutoff function (1 if the condition is true, 0 otherwise).

The methods to calculate σ_{oro} and σ_{rough} yield standard deviations normalized by mean wind speed. Therefore, they first have to be "de-normalized" by multiplication with the corresponding grid cell's mean wind speed (the same that was used in the normalization). Since the mean wind speeds used for roughness and orography differ slightly, we use these two different speeds before adding them together, see Eq. (A.7). Next, the effective increase in wind speed at hub height H has to be calculated:

$$\frac{2\Delta e(H)}{\rho} = (\overline{u}(H) + \Delta u)^3 - \overline{u}(H)^3 \overset{!}{=} 3\overline{u}(H)\sigma^2 \tag{A.5}$$

$$\Rightarrow \Delta u = \overline{u}(H)\left(\sqrt[3]{1+3\sigma_{\text{norm}}^2}-1\right) \tag{A.6}$$

$$\text{with} \quad \sigma_{\text{norm}}^2 = \frac{\sigma_{\text{oro,norm}}^2 \cdot \overline{u}_{\text{oro}}^2 + \sigma_{\text{rough,norm}}^2 \cdot \overline{u}_{\text{rough}}^2}{\overline{u}^2} \tag{A.7}$$

If only the best spots in each grid cell are considered as potential wind sites (i.e. we work with Eq. (A.4) instead of (A.2)), the corresponding wind speed correction takes the following form:

$$\begin{aligned}\Delta u = \frac{\overline{u}}{N}\Bigg\{ & \cdot 3 \cdot \frac{1}{\sqrt{2\pi}}\sigma_{\text{norm}} e^{-p^2/(2\sigma_{\text{norm}}^2)} \\ & + 3 \cdot \frac{1}{2}\sigma_{\text{norm}}^2 \left[1 - \frac{2p}{\sqrt{2\pi\sigma_{\text{norm}}^2}} \cdot e^{-p^2/(2\sigma_{\text{norm}}^2)} \operatorname{erf}\left(\frac{p}{\sqrt{2\sigma_{\text{norm}}^2}}\right)\right] \\ & + \sqrt{\frac{2}{\pi}}\sigma_{\text{norm}}^3 \left(1 + \frac{p^2}{2\sigma_{\text{norm}}^2}\right) e^{-p^2/(2\sigma_{\text{norm}}^2)} \Bigg\},\end{aligned} \tag{A.8}$$

$$\text{with} \quad N = \frac{1}{2}\left(1 - \operatorname{erf}\left(\frac{p}{\sqrt{2\sigma_{\text{norm}}^2}}\right)\right), \tag{A.9}$$

where erf is the error function. Wind is upscaled first, before the correction is added, so the final formula reads

$$u_{\text{corrected}}(H) = u(H) + \Delta u. \tag{A.10}$$

Appendix A.2.1. Surface roughness

We closely follow Ref. [34]. As roughness dataset, we use the land cover atlas from the national land cover database for the US from [43]. It gives land use classes with a resolution of 30 m. The land use classes are converted to surface roughness lengths using Table B.7 in Appendix B. From these data, a contribution to wind speed fluctuations for each grid cell is calculated. Then, the surface layer friction velocity, $u_\star$, is obtained by numerically inverting the geostrophic drag law

$$G = \frac{u_\star}{\kappa}\sqrt{\left(\ln\frac{u_\star}{f z_0} - A\right)^2 + B^2}. \tag{A.11}$$

The geostrophic wind G is assumed to be 10 m/s, $\kappa \approx 0.4$ is the Karman constant, $f \approx 10^{-4}$ is the Coriolis frequency (for latitudes of the contiguous US), and A and B are dimensionless parameters which take the values 1.8 and 4.5, respectively, for stable atmospheric conditions (see e.g. [44]). z_0 is again the surface roughness length.

From $u_\star$, the wind speed at height H is calculated by using again a logarithmic scaling law:

$$u(H) = \frac{u_\star}{\kappa}\ln\frac{H}{z_0} \tag{A.12}$$

According to Ref. [34], the contribution to the wind speed standard deviation from this can be calculated as the standard deviation of $u(H)$ (for all points within one grid cell). Normalized by the mean wind speed of the grid cell, Fig. 6 from Ref. [35] shows their corrections for the Columbia Gorge region. Our corresponding data are shown in Fig. A.15, scaled by a factor of 0.6. The agreement seems reasonable. We believe that the need for scaling our results down to match theirs arises from the higher spatial resolution of our data; they use surface roughness input data with a resolution of 500 m.

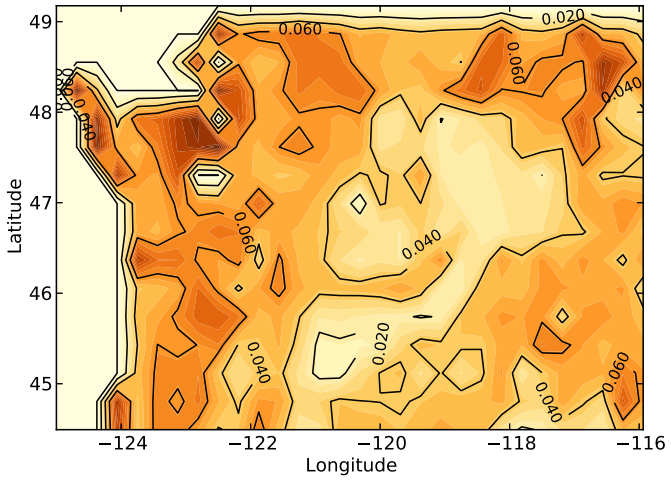

Fig. A.15. Corrections from surface roughness effects from our conversion for the Columbia Gorge region, to compare to Fig. 6 from Ref. [35]. Note that the cutout in this image is not perfectly aligned with the reference image.

Appendix A.2.2. Orography

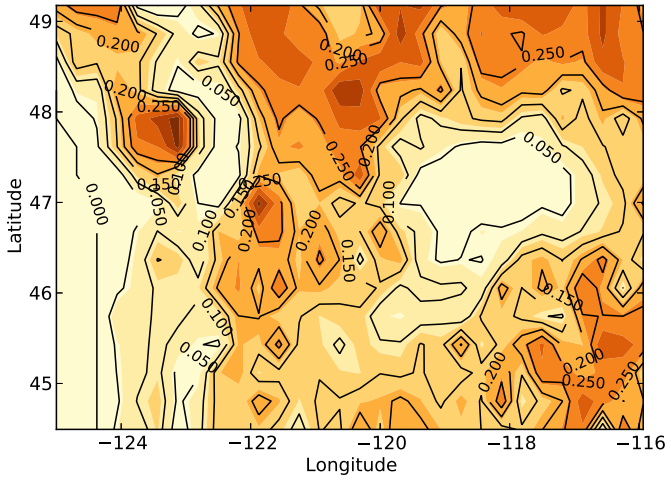

Fig. A.16. Corrections from orography effects from our conversion for the Columbia Gorge region, to be compared to Fig. 5 from Ref. [35]. Note that the cutouts in the two figures are not perfectly aligned.

For orography, the ideas of Ref. [34] are only roughly applied, since the full details of their implementation are, to our knowledge, unpublished. The basic idea is that wind speed-up due to the topography of a landscape should be proportional to its unevenness. As a measure of that, the standard deviation of the elevation, as reported in Ref. [45], is employed. These data have a resolution of 1000 m. When scaled by $(1/3)\cdot(1/8\pi^2)$ (first factor from by-eye fit, second from Ref. [34]) and normalized by the mean wind speed, the agreement with Ref. [35] is reasonable, compare Fig. A.16 to Fig. 5 from Ref. [35].

Appendix A.3. Effect of the corrections

The results of the procedure described above with a choice of $p = 0.84\sigma$ (corresponding to picking the best 20% of the area in each grid cell as eligible for wind farms) are shown in Fig. A.17b and d. Another way to illustrate the effects of the wind speed correction is by looking at plots analogous to Figs. 7–10 from Ref. [35], which show the expected energy yield of each site as calculated from

mean wind speed, mean cubed wind speed, mean cubed wind speed taking the surface roughness and orography corrections into account, and mean wind speed taking the corrections as well as siting effects into account. For our data, these are given in Fig. A.18a–d. The qualitative agreement is reasonable.

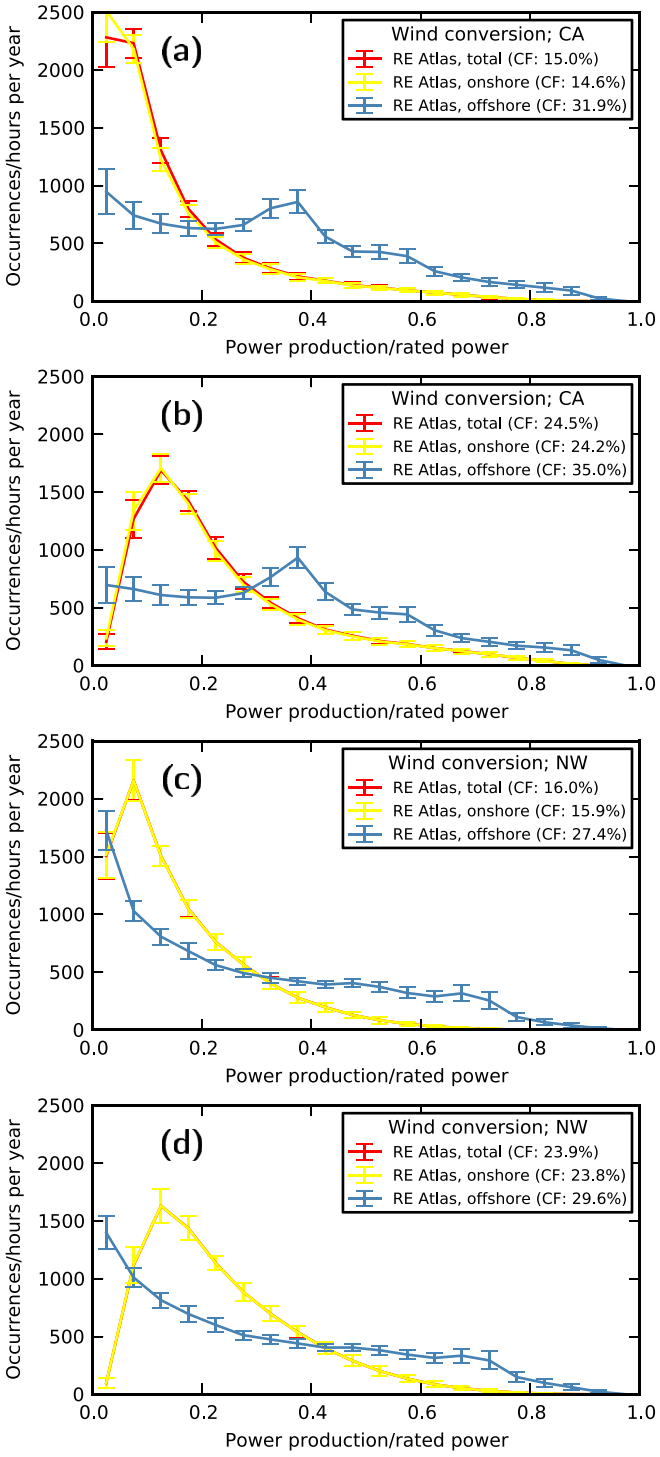

Fig. A.17. The conversions with the RE atlas with and without the corrections are compared. Wind power output histograms without the correction ((a) and (c)), and with the correction ((b) and (d)), including the best 20% of the area within each grid cell, for the California region ((a) and (b)), and the NW FERC region ((c) and (d)). It is obvious that especially onshore, wind power output is systematically underestimated without the correction.

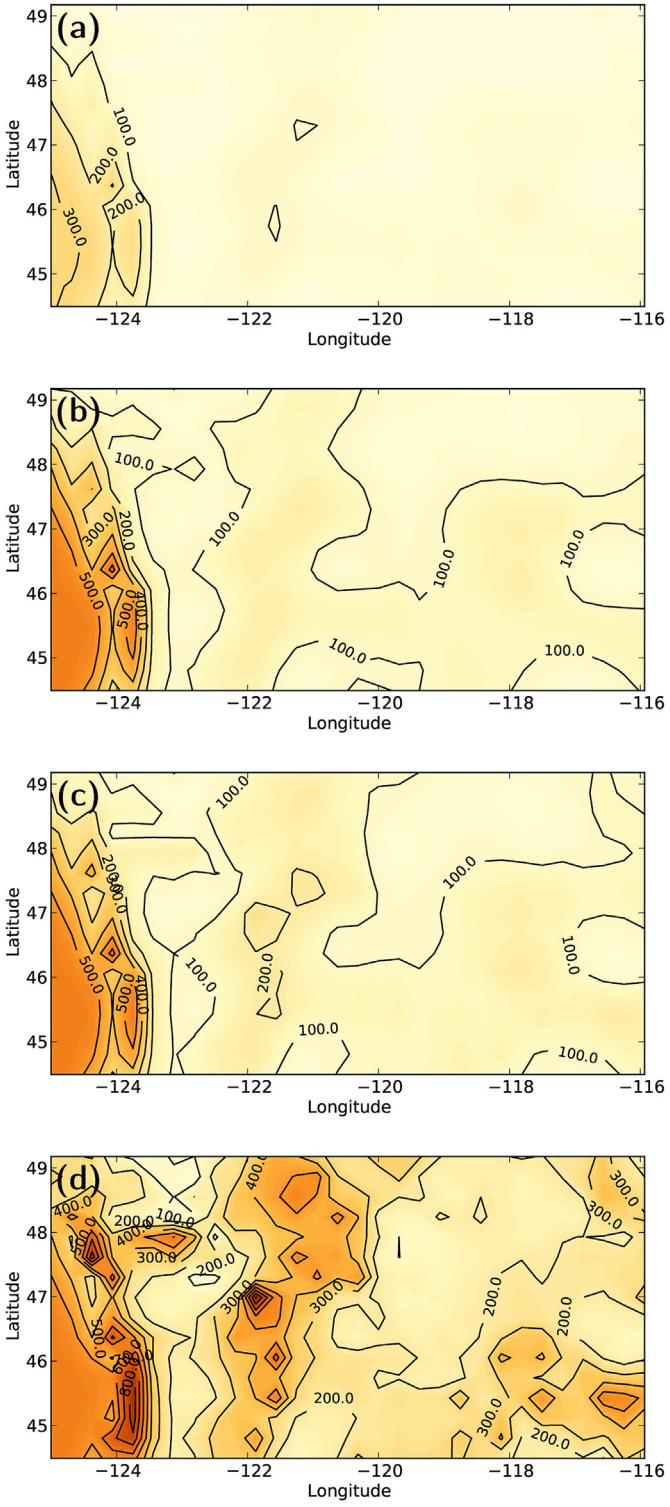

Fig. A.18. Plots analogous to Figs. 7–10 in Ref. [35] for the Columbia Gorge region. Mean wind energy density in 50 m height based on (a) mean wind speed cubed, (b) mean of the cube of the wind speeds, (c) as (b) plus the corrections, including all sites within a grid cell, (d) as (c), but including only the windiest 10% of the wind speed distribution. Color coding is the same in all plots.

Appendix B. Land use to roughness table

Table B.7
Land use–surface roughness relations used for the conversion from the NLCD atlas to surface roughness. Some classes not shown because they only apply to Alaska.

USGS ID	Class	Roughness/m
11	Open Water – All areas of open water, generally with less than 25% cover or vegetation or soil	0.0002
12	Perennial Ice/Snow – All areas characterized by a perennial cover of ice and/or snow, generally greater than 25% of total cover.	0.005
21	Developed, Open Space – Includes areas with a mixture of some constructed materials, but mostly vegetation in the form of lawn grasses. Impervious surfaces account for less than 20% of total cover. These areas most commonly include large-lot single-family housing units, parks, golf courses, and vegetation planted in developed settings for recreation, erosion control, or esthetic purposes.	0.5
22	Developed, Low Intensity – Includes areas with a mixture of constructed materials and vegetation. Impervious surfaces account for 20–49% of total cover. These areas most commonly include single-family housing units.	1
23	Developed, Medium Intensity – Includes areas with a mixture of constructed materials and vegetation. Impervious surfaces account for 50–79% of the total cover. These areas most commonly include single-family housing units.	1
24	Developed, High Intensity – Includes highly developed areas where people reside or work in high numbers. Examples include apartment complexes, row houses and commercial/industrial. Impervious surfaces account for 80–100% of the total cover.	2
31	Barren Land (Rock/Sand/Clay) – Barren areas of bedrock, desert pavement, scarps, talus, slides, volcanic material, glacial debris, sand dunes, strip mines, gravel pits and other accumulations of earthen material. Generally, vegetation accounts for less than 15% of total cover.	0.03
41	Deciduous Forest – Areas dominated by trees generally greater than 5 m tall, and greater than 20% of total vegetation cover. More than 75% of the tree species shed foliage simultaneously in response to seasonal change.	1
42	Evergreen Forest – Areas dominated by trees generally greater than 5 m tall, and greater than 20% of total vegetation cover. More than 75% of the tree species maintain their leaves all year. Canopy is never without green foliage. Enumerated_Domain_Value_Definition_Source: NLCD Legend Land Cover Class Descriptions	1
43	Mixed Forest – Areas dominated by trees generally greater than 5 m tall, and greater than 20% of total vegetation cover. Neither deciduous nor evergreen species are greater than 75% of total tree cover.	0.5
52	Shrub/Scrub – Areas dominated by shrubs; less than 5 m tall with shrub canopy typically greater than 20% of total vegetation. This class includes true shrubs, young trees in an early successional stage or trees stunted from environmental conditions.	0.25
71	Grassland/Herbaceous – Areas dominated by grammanoid or herbaceous vegetation, generally greater than 80% of total vegetation. These areas are not subject to intensive management such as tilling, but can be utilized for grazing.	0.1
81	Pasture/Hay – Areas of grasses, legumes, or grass-legume mixtures planted for livestock grazing or the production of seed or hay crops, typically on a perennial cycle. Pasture/hay vegetation accounts for greater than 20% of total vegetation.	0.03
82	Cultivated Crops – Areas used for the production of annual crops, such as corn, soybeans, vegetables, tobacco, and cotton, and also perennial woody crops such as orchards and vineyards. Crop vegetation accounts for greater than 20% of total vegetation. This class also includes all land being actively tilled.	0.1
90	Woody Wetlands – Areas where forest or shrub land vegetation accounts for greater than 20% of vegetative cover and the soil or substrate is periodically saturated with or covered with water.	0.25
95	Emergent Herbaceous Wetlands – Areas where perennial herbaceous vegetation accounts for greater than 80% of vegetative cover and the soil or substrate is periodically saturated with or covered with water.	0.03

References

[1] Jacobson MZ, Delucchi MA. A Path to Sustainable Energy by 2030. Sci Am 2009;301:58–65.
[2] Archer Cristina L, Jacobson Mark Z. Supplying baseload power and reducing transmission requirements by interconnecting wind farms. J Appl Meteorol Climatol November 2007;46(11):1701–17. http://dx.doi.org/10.1175/2007JAMC1538.1.
[3] Holttinen H. Impact of hourly wind power variations on the system operation in the Nordic countries. Wind Energy 2005;8(2):197–218.
[4] Sinden Graham. Characteristics of the UK wind resource: Long-term patterns and relationship to electricity demand. Energy Policy 2007;35(1):112–27.
[5] Wiemken E, Beyer HG, Heydenreich W, Kiefer K. Power characteristics of PV ensembles: experiences from the combined power production of 100 grid connected PV systems distributed over the area of Germany. Solar Energy 2001;70(6):513–8.
[6] Mills Andrew, Wiser Ryan. Implications of wide-area geographic diversity for short- term variability of solar power. Technical report. Lawrence Berkeley National Laboratory; September 2010., http://emp.lbl.gov/publications/implications-wide-area-geographic-diversity-short-term-variability-solar-power.
[7] Widén J. Correlations between large-scale solar and wind power in a future scenario for Sweden. IEEE Trans Sust Energy 2011;2(2):177–84.
[8] Kempton Willett, Pimenta Felipe M, Veron Dana E, Colle Brian A. Electric power from offshore wind via synoptic-scale interconnection. Proc Natl Acad Sci U S A 2010;107(16):7240–5.
[9] Østergaard Poul A. Geographic aggregation and wind power output variance in Denmark. Energy 2008;33(9):1453–60. http://dx.doi.org/10.1016/j.energy.2008.04.016.
[10] Corcoran BA, Jenkins N, Jacobson MZ. Effects of aggregating electric load in the United States. Energy Policy 2012;46:399–416. http://dx.doi.org/10.1016/j.enpol.2012.03.079.
[11] Hart Elaine K, Jacobson Mark Z. A Monte Carlo approach to generator portfolio planning and carbon emissions assessments of systems with large penetrations of variable renewables. Renew Energy 2011;36(8):2278–86. http://dx.doi.org/10.1016/j.renene.2011.01.015.
[12] Budischak Cory, Sewell DeAnna, Thomson Heather, Mach Leon, Veron Dana E, Kempton Willett. Cost-minimized combinations of wind power, solar power and electrochemical storage, powering the grid up to 99.9% of the time. J Power Sources 2013;225(0):60–74. http://dx.doi.org/10.1016/j.jpowsour.2012.09.054.
[13] Nelson James, Johnston Josiah, Mileva Ana, Fripp Matthias, Hoffman Ian, Petros-Good Autumn, et al. High-resolution modeling of the western North American power system demonstrates low-cost and low-carbon futures. Energy Policy 2012;43:436–47. http://dx.doi.org/10.1016/j.enpol.2012.01.031.
[14] Hand MM, Baldwin S, DeMeo E, Reilly JM, Mai T, Arent D, Porro G, Meshek M, Sandor D. Renewable electricity futures study, vol. 4; 2012. NREL/TP-6A20-52409, http://www.nrel.gov/analysis/re_futures/; 2012.
[15] Lund Henrik, Mathiesen Brian V. Energy system analysis of 100% renewable energy systems – The case of Denmark in years 2030 and 2050. Energy 2009;34(5):524–31. http://dx.doi.org/10.1016/j.energy.2008.04.003.
[16] Connolly David, Lund Henrik, Mathiesen Brian V, Pican Emmanuel, Leahy Martin. The technical and economic implications of integrating fluctuating renewable energy using energy storage. Renew Energy 2012;43:47–60. http://dx.doi.org/10.1016/j.renene.2011.11.003.
[17] Schaber K, Steinke F, Hamacher T. Transmission grid extensions for the integration of variable renewable energies in Europe: who benefits where? Energy Policy February 2012;43:123–35.
[18] Schaber K, Steinke F, Hamacher T, Mühlich P. Parametric study of variable renewable energy integration in Europe: advantages and costs of transmission grid extensions. Energy Policy December 2011;42:498–508.
[19] Heide D, von Bremen L, Greiner M, Hoffmann C, Speckmann M, Bofinger S. Seasonal optimal mix of wind and solar power in a future, highly renewable Europe. Renew Energy November 2010;35:2483–9.
[20] Heide D, Greiner M, von Bremen L, Hoffmann C. Reduced storage and balancing needs in a fully renewable European power system with excess wind and solar power generation. Renew Energy September 2011;36:2515–23.

[21] Rasmussen MG, Andresen GB, Greiner M. Storage and balancing synergies in a fully or highly renewable pan-European power system. Energy Policy December 2012;51:642–51.
[22] Rodriguez RA, Becker S, Andresen GB, Heide D, Greiner M. Transmission needs across a fully renewable European power system. Renew Energy March 2014;63:467–76. http://arxiv.org/abs/1306.1079. preprint available at, http://dx.doi.org/10.1016/j.renene.2013.10.005.
[23] Becker S, Rodriguez RA, Andresen GB, Schramm S, Greiner M. Transmission grid extensions during the build-up of a fully renewable pan-European electricity supply. Energy January 2014;64:404–18. preprint available at, http://arxiv.org/abs/1307.1723.
[24] Elliston Ben, Diesendorf Mark, MacGill Ian. Simulation of scenarios with 100 % renewable electricity in the Australian National Electricity Market. Energy Policy March 2012;45:606–13. http://dx.doi.org/10.1016/j.enpol.2012.03.011.
[25] Elliston Ben, MacGill Iain, Diesendorf Mark. Comparing least cost scenarios for 100% renewable electricity with low emission fossil fuel scenarios in the Australian National Electricity Market. Renew Energy 2014;66(0):196–204. http://dx.doi.org/10.1016/j.renene.2013.12.010.
[26] Søndergaard AA. Development of a renewable energy atlas and extreme event analysis in renewable energy systems. M.Sc. thesis. Denmark: Aarhus University; 2013.
[27] Saha Suranjana, Moorthi Shrinivas, Pan Hua-Lu, Wu Xingreni, Wang Jiande, Nadiga Sudhir, et al. The NCEP climate forecast system reanalysis. Bull Am Meteor Soc April 2010;91(8):1015–57. http://dx.doi.org/10.1175/2010BAMS3001.1.
[28] Solar panel data. ; 2012 http://www.scheutensolar.de; 2012. Online, retrieved 2012.
[29] Wind and solar resource maps. ; 2013. Online [accessed Nov 2013], http://www.nrel.gov/gis/maps.html; 2013.
[30] Brower Michael, for NREL, under supervision of D. Corbus. Development of eastern regional wind resource and wind plant output datasets. Technical report. Albany, New York: AWS Truewind LLC; 2009. Final data sets available at:, http://www.nrel.gov/electricity/transmission/eastern_wind_dataset.html.
[31] Potter C, Nijssen B, for NREL, under supervision of D. Lew. Development of regional wind resource and wind plant output datasets. Technical report. Seattle, Washington: 3TIER; 2009. Final data sets available at:, http://www.nrel.gov/electricity/transmission/western_wind_dataset.html.
[32] Archer CL, Jacobson MZ. Spatial and temporal distributions of U.S. winds and wind power at 80 m derived from measurements. J Geophys Res 2003;108(D9):4289. http://dx.doi.org/10.1029/2002JD002076.
[33] Turbine overview. Online, retrieved 2011, http://www.vestas.com/en/wind-power-plants/procurement/turbine-overview.aspx; 2011.
[34] Badger J, Kelly MC, Jørgensen HE. Regional wind resource distributions: mesoscale results and importance of microscale modeling. ; 2010. Online publication of conference talk slides, retrieved May 2013, http://emf.stanford.edu/events/snowmass_2010/; 2010.
[35] Badger J, Jørgensen HE. A high resolution global wind atlas – improving estimation of world wind resources. In: Risø international energy conference 2011; 2011. pp. 215–25.
[36] Technical report Cost and performance review of generation technologies: recommendations for WECC 10- and 20-year studies. San Francisco, CA: Energy and Environmental Economics (E3); 2012. Online, retrieved Aug 2013, http://www.nwcouncil.org/media/6867814/E3_GenCapCostReport_finaldraft.pdf.
[37] US Army Corps of Engineers. Civil works construction cost index system. Technical report. US Army Corps of Engineers; 2011., http://planning.usace.army.mil/toolbox/library/EMs/em1110.2.1304.pdf. Online, retrieved Aug 2013.
[38] Transparent cost database.http://en.openei.org/apps/TCDB/; 2013. Online, retrieved Aug 2013.
[39] Short W, Sullivan P, Mai T, Mowers M, Uriarte C, Blair N, Heimiller D, Martinez A. Regional Energy Deployment System (ReEDS). Technical report. Golden, Colorado: National Renewable Energy Laboratory (NREL); December 2011. Report available at:, http://www.nrel.gov/analysis/reeds/documentation.html.
[40] Kirkpatrick S, Gelatt CD, Vecchi MP. Optimization by simulated annealing. Science 1983;220(4598):671–80. http://dx.doi.org/10.1126/science.220.4598.671.
[41] Černý V. Thermodynamical approach to the traveling salesman problem: an efficient simulation algorithm. Journal of Optimization Theory and Applications 1985;45(1):41–51. http://dx.doi.org/10.1007/BF00940812.
[42] Delucchi Mark A, Jacobson Mark Z. Providing all global energy with wind, water, and solar power, part II: reliability, system and transmission costs, and policies. Energy Policy 2011;39(3):1170–90. http://dx.doi.org/10.1016/j.enpol.2010.11.045.
[43] Fry J, Xian G, Jin S, Dewitz J, Homer C, Yang L, Barnes C, Herold N, Wickham J. Completion of the 2006 national land cover database for the conterminous United States. Technical report. Multi-resolution Land Characteristics Consortium; 2011., http://www.mrlc.gov/nlcd2006.php. Online, retrieved May 2013.
[44] Petersen EL, Mortensen NG, Landberg L, Højstrup J, Frank HP. Wind power meteorology. Roskilde, Denmark: Risø National Laboratory; 1997.
[45] North America digital elevation model raster dataset. Redlands, CA: ESRI; 2005. Technical report, http://webhelp.esri.com/arcgisdesktop/9.1/body.cfm?tocVisable=1&ID=2109&TopicName=North%20America%20Digital%20Elevation%20Model.